

## Supplementary Material

### Samples and Methods

The Upper Pumice (UP) and Post Caldera Dome (PCD) samples have been collected during two main field campaigns in 2006 and 2014 as described in Braschi et al., 2012 and 2022. A total amount of 72 samples (11 lava domes and 61 enclaves) for PCD and 94 samples for the UP tephra (9 pumice and 22 Crystal Rich Clasts -CRCs-) were sampled and analyzed for major, trace elements and isotopes (all data are reported in Braschi et al., 2012 and Mastroianni et al., 2022). The selected samples chosen for mineral chemistry investigations are detailed in Table S1; results are reported in Table S2a-f.

Mineral chemistry analyses were performed at the microprobe laboratory of the CNR-IGG of Florence. The instruments used was a JEOL Superprobe JXA8600 equipped with 4 wavelength dispersion spectrometers. Analytical condition was 15 kV accelerating voltage, 10 nA beam current and focused beam, except for feldspar and glasses where the beam was defocused to 5  $\mu$ m and 10  $\mu$ m respectively, to reduce diffusion effect on alkali.

Peak counting times were 15s for major elements and 30-40s for minor elements, except for Na which was measured for 10s at the beginning of each analysis to minimize element migration. Background counting times were 50% of peak counting times. The Bence & Albee, (1968) algorithm was used for matrix effect correction.

A selection of Astimex natural and synthetic phases was used as primary standard for the elemental calibration. Several natural mineral phases are used as secondary quality-control standards (Smithsonian Olivine San Carlos, Augite Kakanui, Ilmenite and Diopside, Astimex Albite, Plagioclase, Apatite). The accuracy of the method is better than 3% for all elements whereas precision ( $\sigma$ ) is better than 3% for major elements (>1 wt.%) and between 5-10% for minor elements (0.1.-1 wt.%) based on repeated (more than 100) analyses of the secondary standards, as reported in Vaggelli et al. (1999), providing significant values on the second and third digits, respectively.

The new JEOL JXA8230 microprobe installed at the joined laboratory of the CNR-IGG and Department of Earth Sciences of the University of Florence was recently used to integrate the dataset for some samples and to acquire back scattered (BSE) images of representative analytical sites. The new instrument is equipped with 5 wavelength dispersion spectrometers and operated with the same analytical conditions than the old one except for the probe current on femic phases that was set to 20 nA. In this case the applied matrix effect correction followed the ZAF method. Calibration standards were the same than in the old microprobe and secondary standards gave

comparable results in terms of average and confidence intervals, avoiding the need of cross corrections for data comparison during time (Table S2g).

For geothermobarometer application analyses were accurately checked and selected, discarding those with low closure or bad stoichiometry. The results obtained by the application of Chicchi et al., (2023) geo-thermobarometer on clinopyroxene is reported in Table S3 and those obtained by the application of Higgins et al., (2022) on amphiboles are reported in Table S4.

## Literature

Bence, AE, Albee, AL, Empirical correction factors for the electron microanalysis of silicates and oxides. *J Geol*, 76:382–402, 1968.

Braschi, E., Francalanci, L., and Vougioukalakis, G.E.: Inverse differentiation pathway by multiple mafic magma refilling in the last magmatic activity of Nisyros Volcano, Greece, *Bull. Volcanol.*, 74, 1083–1100, <https://doi.org/10.1007/s00445-012-0585-1>, 2012.

Braschi, E., Mastroianni, F., Di Salvo, S., Agostini, S., Vougioukalakis, G.E., Francalanci, L., Unveiling the occurrence of transient, multi-contaminated mafic magmas inside a rhyolitic reservoir feeding an explosive eruption (Nisyros, Greece), *Lithos* 410–411, 10657, doi: 10.1016/j.lithos.2021.106574, 2022.

Chicchi, L., Bindi, L., Fanelli, D., and Tommasini, S.: Frontiers of thermobarometry: GAIA, a novel Deep Learning-based tool for volcano plumbing systems, *Earth Planet. Sci. Lett.*, 620, 118352, <https://doi.org/10.1016/j.epsl.2023.118352>, 2023.

Mastroianni, F., Braschi, E., Agostini, S., Di Salvo, S., Casalini, M., Vougioukalakis, G., Francalanci, L., 2021. Data on: Unveiling the Occurrence of Transient, Multi- Contaminated Mafic Magmas Refilling a Rhyolitic Reservoir in a Explosive Eruptions (Nisyros, Greece). Data in Brief, submitted.

Higgins, O., Sheldrake, T., and Caricchi, L.: Machine learning thermobarometry and chemometry using amphibole and clinopyroxene: a window into the roots of an arc volcano (Mount Liamuiga, Saint Kitts), *Contributions to Mineralogy and Petrology*, 177 (10), <https://doi.org/10.1007/s00410-021-01874-6>, 2022.

Vaggelli, G., Olmi, F., Conticelli, S.: Evaluation of analytical errors during microprobe analyses of silicate minerals international reference samples, *Acta Vulcanol*, 11:297, 303, 1999.

## Supplementary Figures

Figure S1

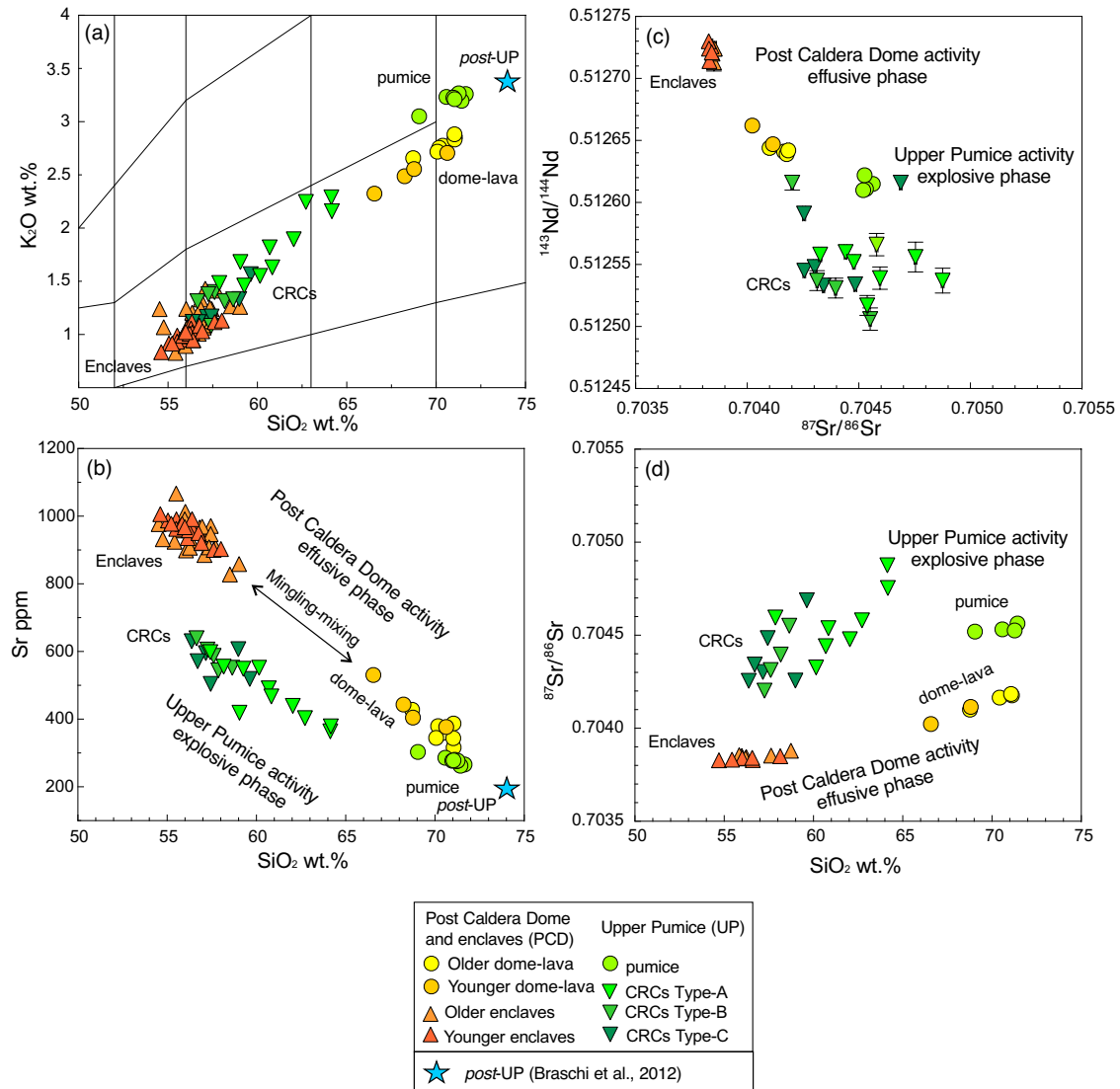


Figure S1 – compositional diagrams showing and comparing the main geochemical and isotopic characteristics of the UP and PCD juveniles. a: Classification diagram  $K_2O$  vs  $SiO_2$  (wt.%); b: Sr ppm vs  $SiO_2$  wt.%. The strong enrichment in Sr content of the PCD-enclaves with respect to CRCs clearly indicates the different nature of the two magmas; c: Sr vs Nd isotopes plot; d:  $^{87}Sr/^{86}Sr$  vs  $SiO_2$  correlation plot. The Sr-Nd isotopes further highlight the different genesis of the magmas forming the CRCs and PCD-enclaves. CRCs show complex variations with a large range of  $^{87}Sr/^{86}Sr$  and  $^{143}Nd/^{144}Nd$ , that reach the lowest values observed for Nisyros mafic magmas, testifying for peculiar differentiation processes (Braschi et al., 2022). On the contrary PCD-enclaves have a more homogeneous signature with low  $^{87}Sr/^{86}Sr$  and high  $^{143}Nd/^{144}Nd$ , typical of mantle derived magmas (Braschi et al., 2012). Symbols discriminate the different lithologies, whereas colors discriminate the two different activities. Green shadows account for the different CRCs types based on textures, as detailed in legend. Yellow and orange shadows relate to the different time of emplacement for the PCDs according to Vougioukalakis (1993) and Dietrich (2018) and supported by geochemical, textural and mineralogical evidence provided in Braschi et al. (2012).

Figure S2

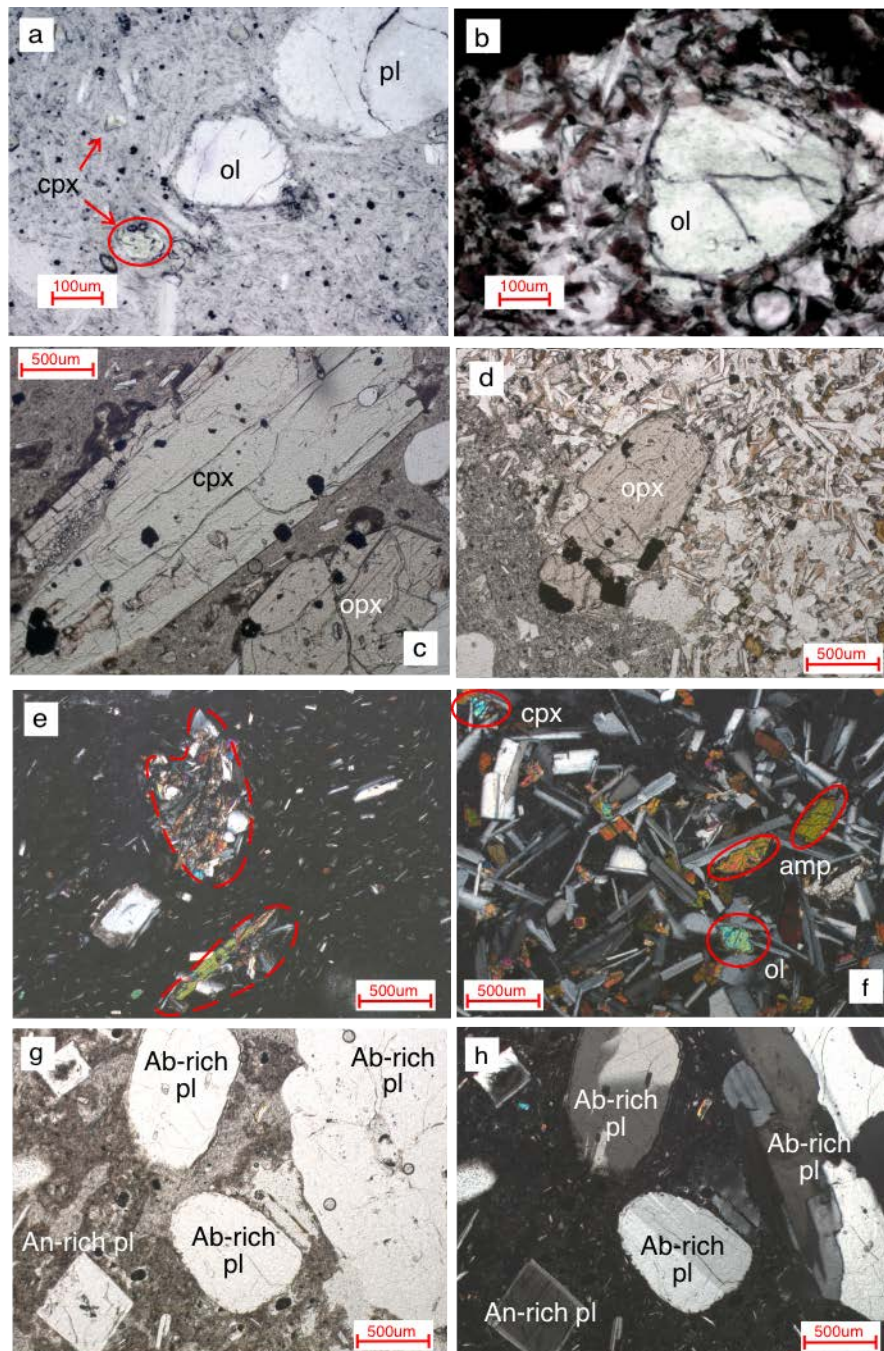


Figure S2 – Microscope picture of some petrographic details in the PCD samples. a: plane polarized light micro-photograph of a rare olivine (ol) micro-phenocrysts in PCD lavas and b: in the enclaves; c: plane polarized light micro-photograph of clinopyroxene (cpx) and orthopyroxene (opx) phenocrysts with aggregated oxides in the PCD lavas; d: light polarized light micro-photograph of an orthopyroxene phenocryst escaping from an enclave into the host lavas, demonstrating that enclaves are discrete batch inside the host but behave plastic until eruption; e: crossed polarized light micro-photograph of two micro-enclaves dispersed into the cryptocrystalline groundmass of PCD lavas; f: crossed polarized light micro-photograph of the enclave dictytaxitic texture with interstitial clinopyroxene and olivine; g-h: plane and crossed polarized light micro-photograph of Anorthite-rich (An-rich) and Albite-rich (Ab-rich) plagioclase (pl) phenocrysts in a PCD lava.



Figure S3

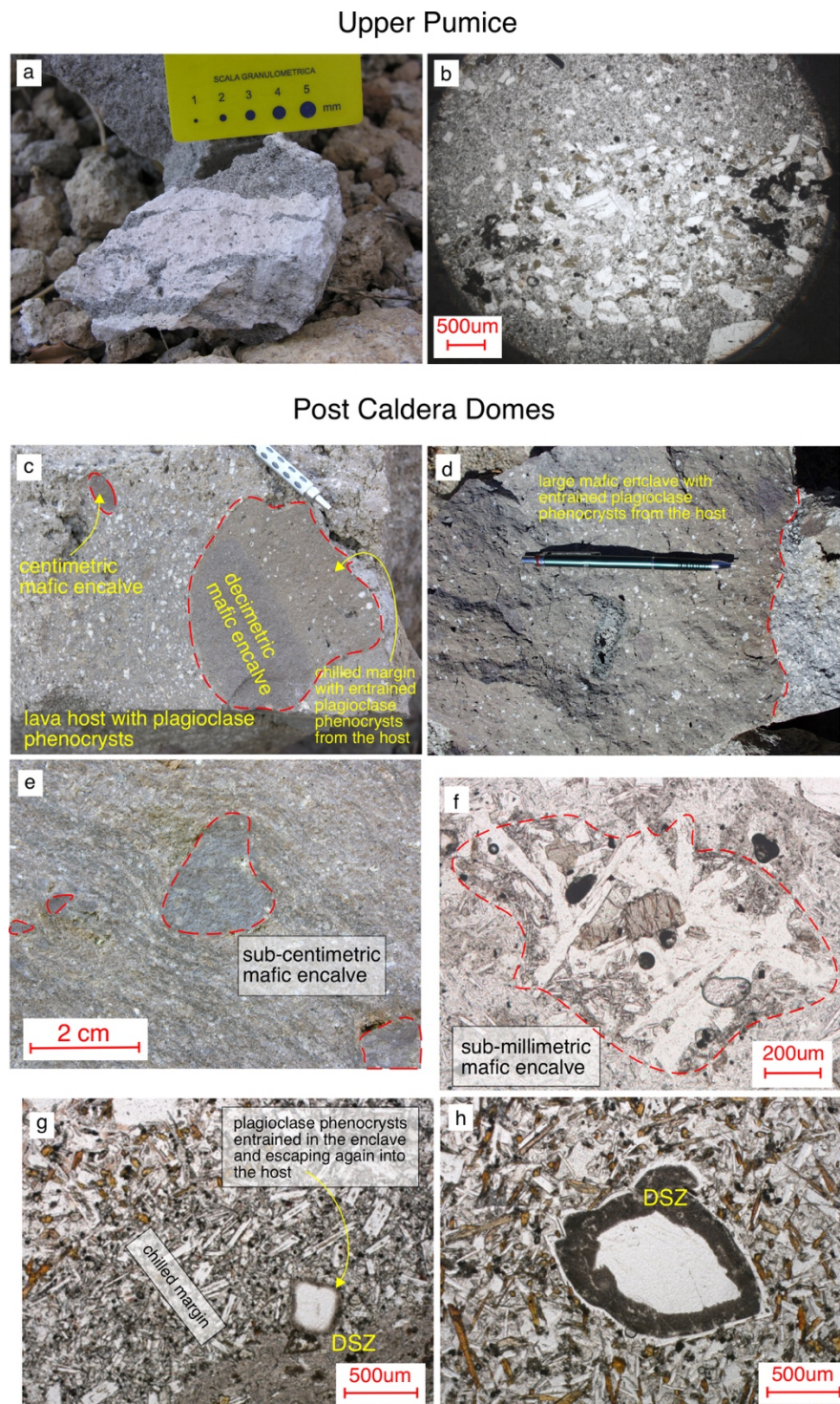


Figure S3 – Hand specimen and microscope pictures showing the contacts between the two lithologies originated by the magma interaction during the UP (a-b) and PCD (c-e) activities. The progressive enclave disaggregation from macro (c, d) to micro scale (e, f) and single crystal exchange (g) between post-caldera lava domes and enclaves. In c and f picture the chilled margin is particularly evident for the PCD-enclaves, as well as the occurrence of plagioclase phenocrysts coming from the host. Plagioclase phenocrysts from the host dome lavas may be indeed entrapped within the enclaves (h) where undergo partial dissolution due to the higher temperature of the mafic melt, forming dusty sieved zone (DSZ) of different extension and, if time is enough a clear (equilibrium) outer rim.

Figure S4

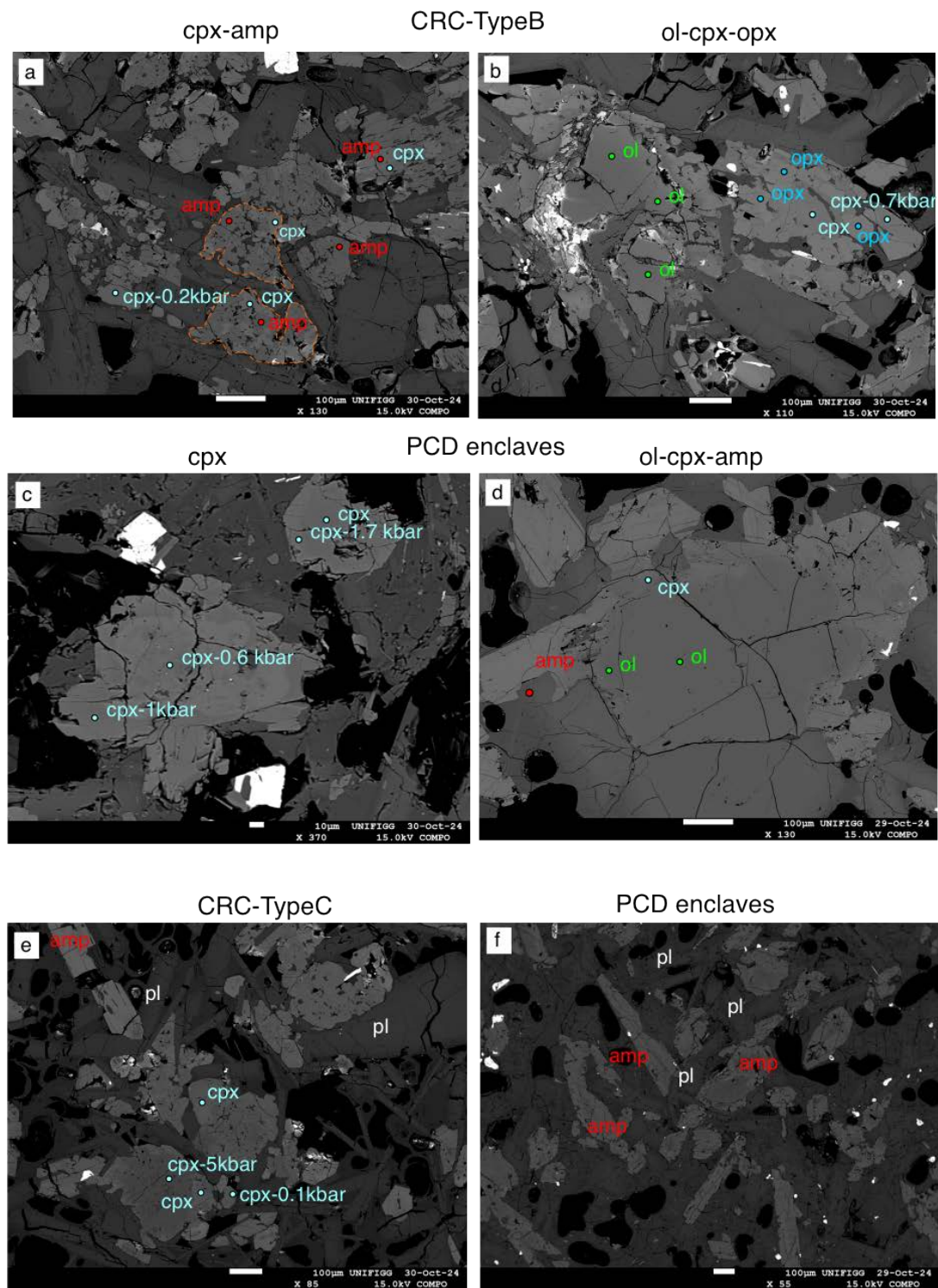


Figure S4 – Backscattered images showing in detail a: the relationships between clinopyroxenes (cpx) and amphiboles (amp) and b: between olivines (ol), orthopyroxenes (opx) and clinopyroxenes in the CRCs; c: the clinopyroxene textures and d: the relationships between olivine, clinopyroxene and amphibole in the PCD enclaves. In e and f the comparison between the dictyotaxitic texture of amphiboles and plagioclase (pl) in the CRCs Type-C and the PCD enclaves is shown.



Figure S5

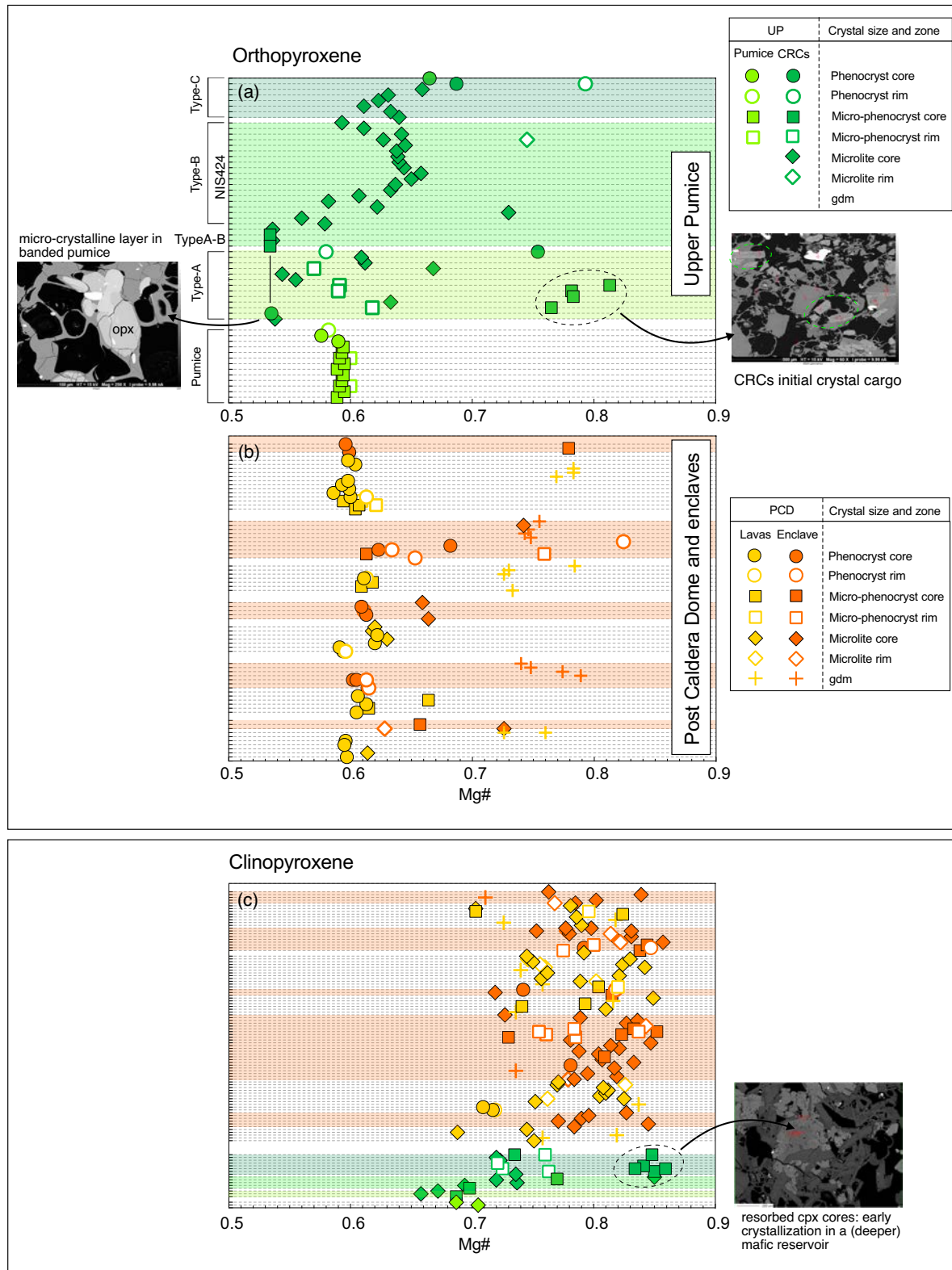


Figure S5 – Core-rim Mg# variations in orthopyroxene of the UP (pumice and CRCs) (a) and the PDC (host lavas and enclaves) (b) compared to clinopyroxene (c). Each single crystal is reported along the same horizontal line to show the zoning pattern. Composition of groundmass (gdm) is also shown. BSE images refer to specific cases as identified by arrows.

Figure S6

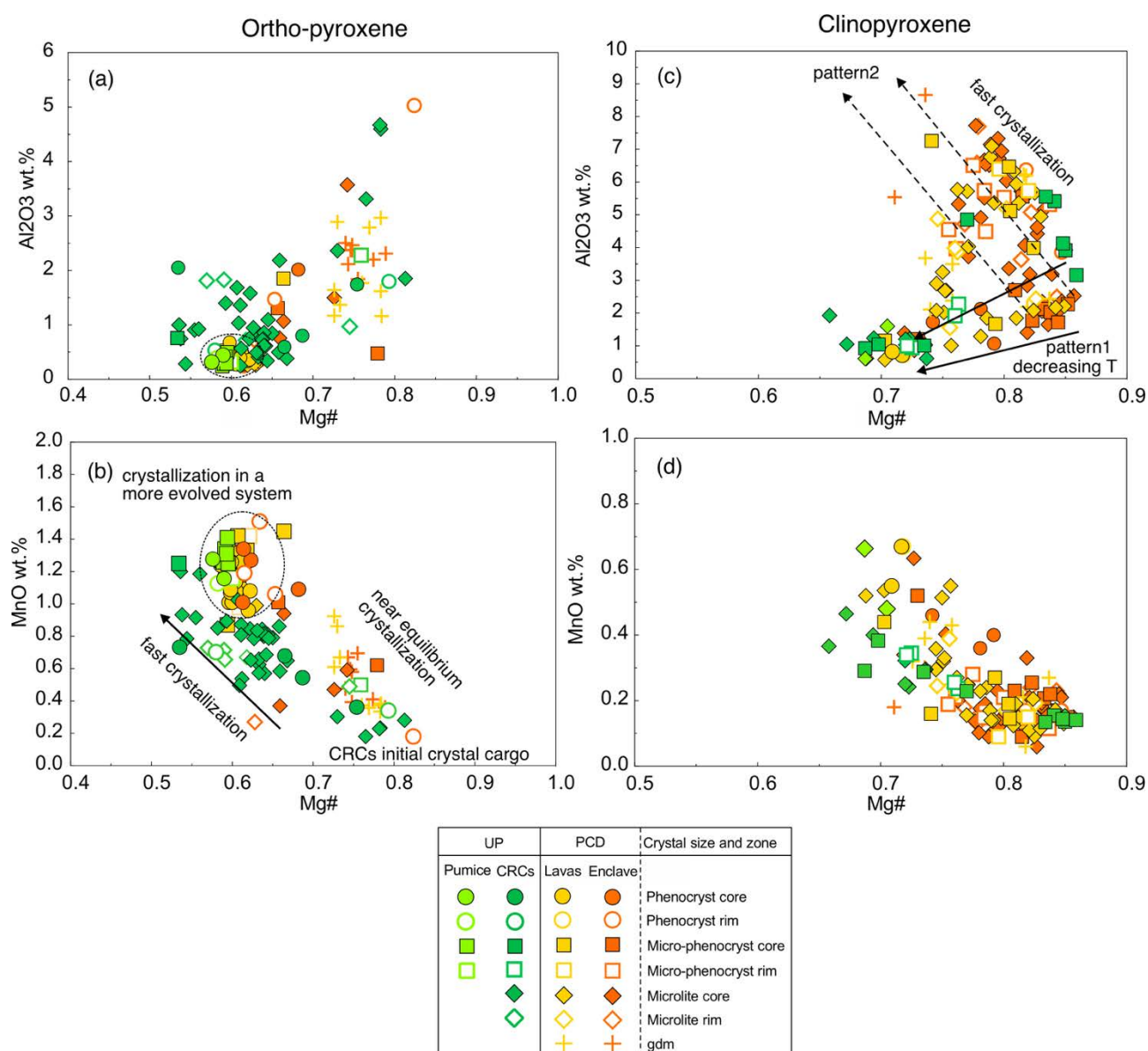


Figure S6 – correlation diagram showing the ortho (a,b) and clinopyroxenes (c,d) compositional variability and trends using Al<sub>2</sub>O<sub>3</sub> wt.% (a,c) and MnO wt.% versus Mg# (b,d) for the UP and PCD juveniles. In (c) pattern 1 represents crystallization in an evolving system where plagioclase crystallize together with clinopyroxene; pattern 2 represents crystallization in a system where plagioclase crystallization has not yet begun. The detection limit is 0.09 wt.% for MnO and 0.1 wt.% for Al<sub>2</sub>O<sub>3</sub> considering 40 sec and 15 sec of peak counting time, respectively. Replicates on reference standards show a good precision with standard deviations lower than 3% for many major elements (>1 wt.%) such as Al<sub>2</sub>O<sub>3</sub> and 5% for minor elements (0.1-1 wt.%) such as MnO, providing significant values on the second and third digits, respectively. The standard deviation ( $\sigma$ ) is in the range between 0.1 and 0.6 and 0.02 and 0.06 for major and minor elements, respectively (see Table S2g and Vaggelli et al., 1999 for reference). The representative error is similar to the size of symbols.



Figure S7

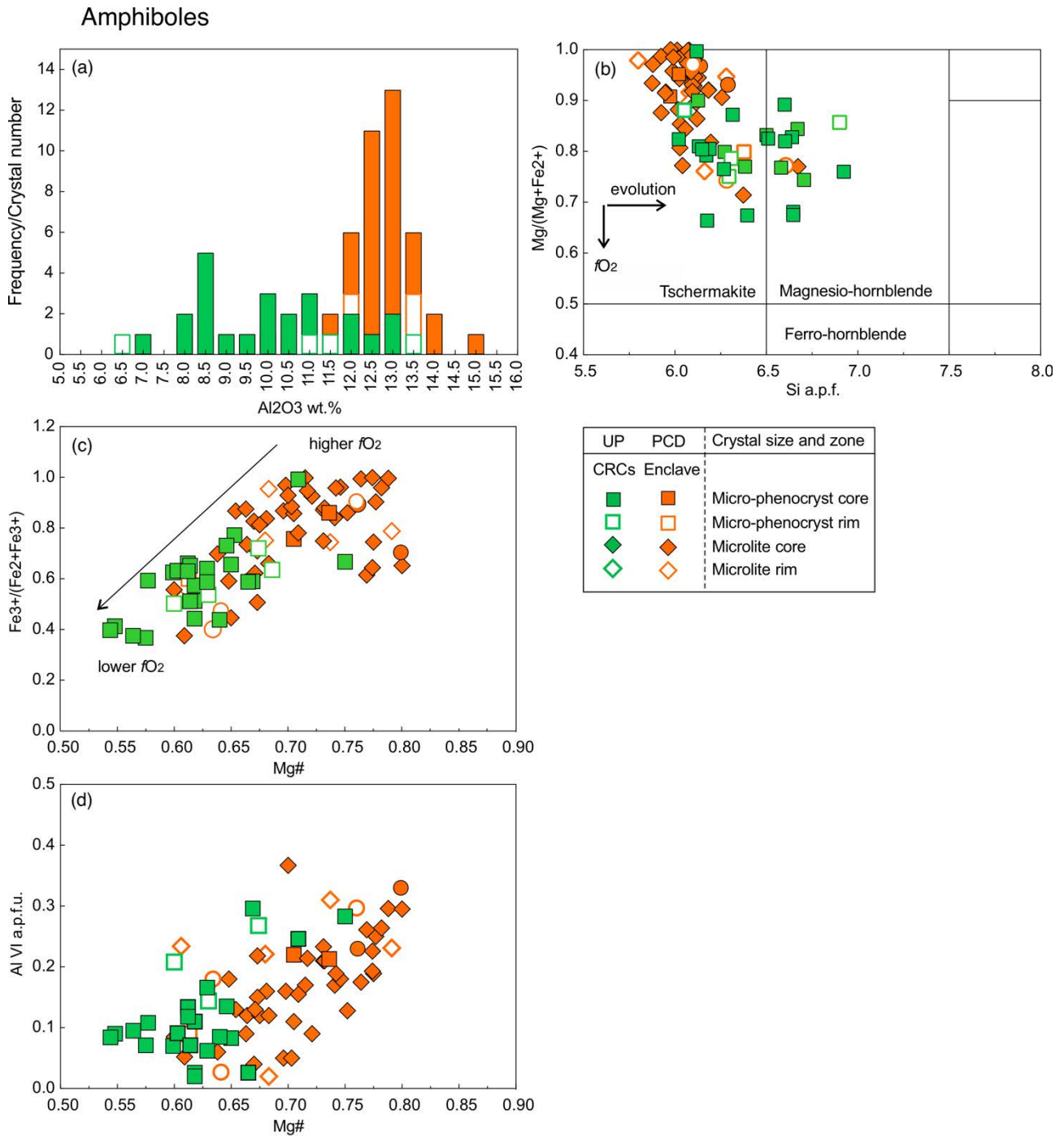


Figure S7 – a: histogram of  $\text{Al}_2\text{O}_3$  wt.% core-rim composition in the CRCs and PCD-enclaves amphiboles; b: classification diagram for the analyzed amphiboles; c: correlation diagram between  $\text{Fe}^{3+}/(\text{Fe}^{2+}+\text{Fe}^{3+})$  and  $\text{Mg}\#$  highlighting the effects of  $f\text{O}_2$  on amphibole composition; d: correlation diagram between the T and  $f\text{O}_2$  sensitive  $\text{Al}^{\text{VI}}$  and  $\text{Mg}\#$ .

Figure S8

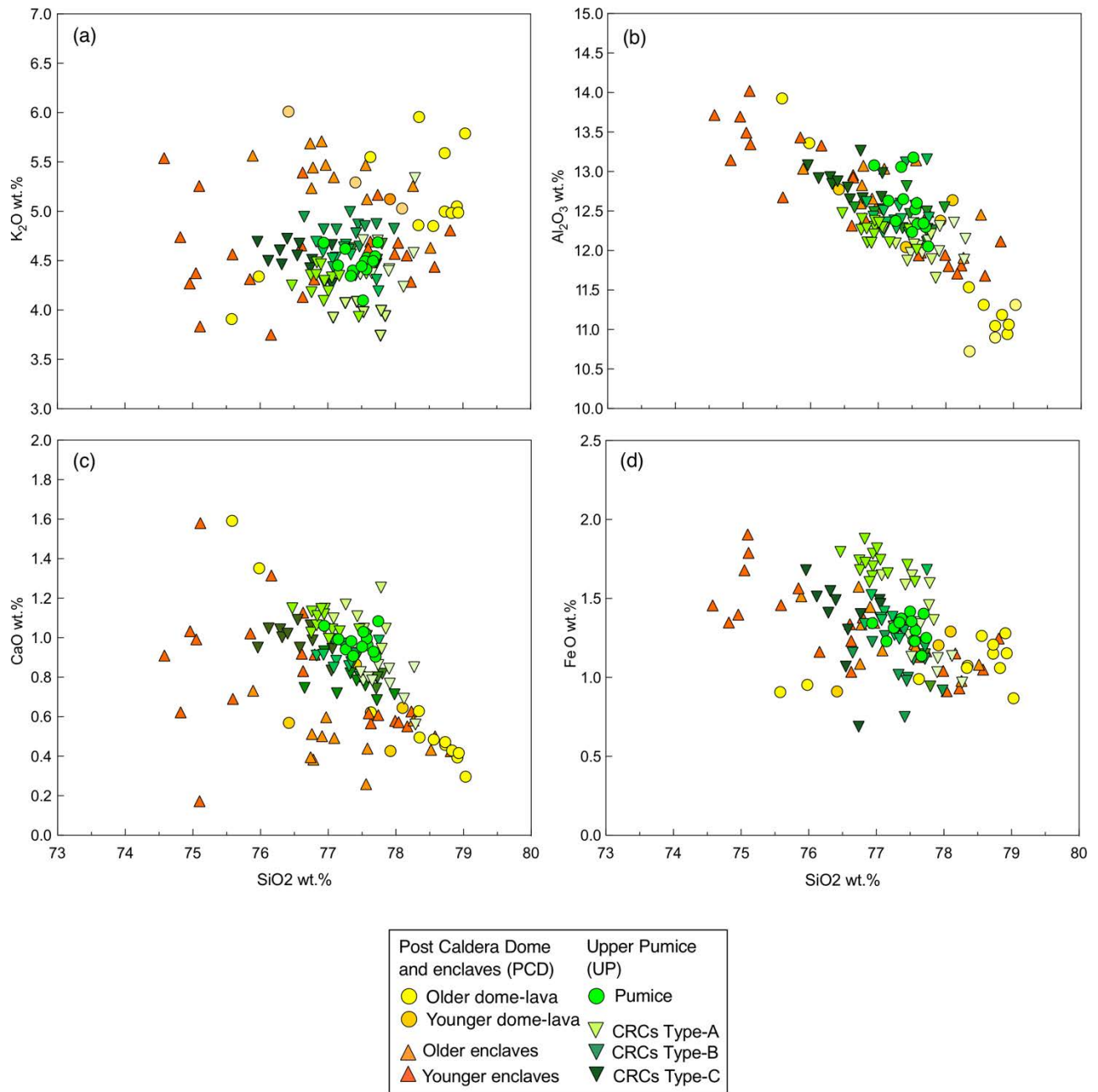


Figure S8 – Representative compositional diagrams of glasses analyzed in the UP and PCD products. a: K<sub>2</sub>O wt.%, b: Al<sub>2</sub>O<sub>3</sub> wt.%, c: CaO wt.% and d: FeO wt.% vs silica. Notably, glasses of the PCD-enclaves are more variable in composition with respect to CRCs, similarly those of the PCD-lavas reveal some scattered composition, especially for K<sub>2</sub>O and FeO at lower silica content than UP-pumice.